Micromechanics-guided development of a slag/fly ash-based strain-hardening geopolymer composite
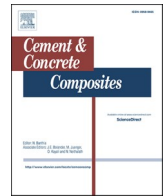
Zhang, Shizhe; Li, Victor C.; Ye, Guang

Important note
To cite this publication, please use the final published version (if applicable).
Please check the document version above.

Micromechanics-guided development of a slag/fly ash-based strain-hardening geopolymer composite

Shizhe Zhang [a], Victor C. Li [b,*], Guang Ye [a,**]

[a] *Microlab, Section Materials and Environment, Faculty of Civil Engineering and Geosciences, Delft University of Technology, Stevinweg 1, 2628 CN, Delft, the Netherlands*
[b] *Department of Civil and Environmental Engineering, University of Michigan, Ann Arbor, MI, 48109, USA*

ARTICLE INFO

ABSTRACT

Strain-hardening geopolymer composite (SHGC) lately emerged as a promising alternative to traditional strain-hardening cementitious composite with added advantages of industrial by-product utilization and enhanced sustainability. However, as the design of SHGC requires multi-factor optimization, the application of traditional trial-and-error method is inefficient and hinders the development of this material.

This paper aims at the development of a slag/fly ash-based SHGC with low slag content using a micromechanical model to guide the composite mixture design. To this end, experimentally characterized physical properties of fiber, matrix and interface are used as input for the micromechanical model, which serves as a predictive tool for the tensile performance of SHGC. Following the guidance, a slag/fly ash-based SHGC with tensile strain capacity of 4.8% and ultimate tensile strength above 3.8 MPa was systematically developed. The feasibility and effectiveness of using micromechanics as the design basis of SHGC are demonstrated and experimentally verified.

1. Introduction

Engineered cementitious composite (ECC) [1] is a strain-hardening cementitious composite (SHCC) with a micromechanics design basis [2]. Reinforced with only a small volume fraction of randomly distributed short cut fibers, SHCC shows extraordinary tensile strain capacity, which is several hundred times larger than conventional OPC concrete. The added functionality of this material has been further explored for concrete repair applications due to its high ductility and multiple cracking behavior [3,4]. However, the high amount of ordinary Portland cement (OPC) usage in SHCC makes it a high energy embedded product and increases the CO_2 emission, which negatively impacts its sustainability performance. To improve the greenness of SHCC, researchers have partially replaced cement with supplementary cementitious materials (SCMs) to reduce the OPC content [5–7]. Up till now, the industry and scientific communities are still striving for an improvement on a more sustainable approach to make SHCC.

Towards the further enhanced greenness of SHCC, an emerging solution involves the utilization of cement-free alkali-activated binder to replace the traditional cementitious binder as matrix in SHCC. Alkali-activated materials (AAMs) including those classified as geopolymer, which have the potential of transforming different industrial by-products and wastes into cement-free building materials, have emerged as a sustainable and environmentally friendly alternative to the OPC binders. These materials are derived from the reaction of an alkali metal source (solid or dissolved) with a solid (alumino-)silicate powder [8,9]. In comparison to traditional cementitious binders, they maintain comparable and even better performance concerning mechanical properties and durability. Furthermore, it is reported that concrete based on AAMs in comparison with OPC-based concrete can reduce 80% or even higher carbon emissions [10,11]. Additionally, the environmental impact of concrete based on AAMs could be reduced even further if waste-derived activators are used [12]. Up till now, a variety of mineral precursors (e.g., metakaolin) and industrial by-products have been used for AAMs preparation, among which AAMs or geopolymer based on blast furnace slag and class F fly ash are most intensively studied [8,9,13,14]. Previous studies of slag/fly ash-based AAMs have focused on microstructure development, nature of reaction products and mechanical properties [15–19] and its application as binder material for construction has been greatly promoted.

Recently, several types of strain-hardening geopolymer composite (SHGC) developed using different mineral precursors can be found in the literature. For instance, Lee et al. developed a slag-based alkali-activated mortar with tensile strain up to 4.7% [20]. Ohno and Li researched on the feasibility of strain-hardening fly ash-based geopolymer composite and developed a ductile engineered geopolymer composite (EGC) based on two kinds of fly ashes and polyvinyl alcohol (PVA) fiber [21,22]. Furthermore, they also proposed an integrated design method, which includes using a statistical design method for the matrix, micro-mechanical modelling for the composite behavior and determination of sustainability indices for the environmental design [22]. Nematollahi et al. developed SHGC using PVA fibers, including a fly ash-based EGC by heat curing [23,24] and a slag/fly ash-based SHGC cured at ambient temperature [25]. In addition, Nematollahi et al. also investigated the feasibility of using high modulus polyethylene (HMPE) fiber in a one-part SHGC with the added advantage of material handling during preparation [26]. Farooq et al. investigated the tensile performance of several types of eco-friendly ductile geopolymer composite (EDGC) reinforced with different micro-fibers and strain-hardening was achieved by PVA fibers EDGC [27]. Almost all the above-mentioned SHGCs exhibit good strain-hardening behavior (>3%) and multi-cracking characteristics. At the same time, it is proved that the developed SHGC brings tremendous environmental benefit with considerable lower embodied energy and carbon equivalent emissions in comparison with normal SHCC (e.g., M45 [28]) and SHCC with SCMs incorporation (e.g., High volume fly ash ECC [6]) [22,25]. It is important to note that the term geopolymer by its definition strictly relates to a synthetic alkali aluminosilicate material, which is characterized by its three-dimensional aluminosilicate network [8]. However, it seems that the term geopolymer is more frequently used by civil engineers for AAMs especially in the researches with regard to the development of strain-hardening composite. Considering the low slag content (i.e., low Ca content) used for SHGC preparation and the terminology consistency with previous literature, this study adopts the term geopolymer as in strain-hardening geopolymer composite (SHGC).

Despite the outstanding performance of the SHGC in previous studies, challenges still exist regarding the mixture design of SHGC, which involves even more factors to be considered compared to traditional SHCC design [22]. The micromechanical model developed by Li et al. [29,30], providing a solid theoretical design basis, has been used in previous studies on SHGC [25,31]. However, most of these studies, along with studies in SHCC, used this model mainly on already developed mixtures to explain the origin of strain-hardening behavior and sometimes for optimization purposes. Rarely has the micromechanical model served as a predictive tool to guide the design of SHGC from scratch.

The main aim of this work is the development of a slag/fly ash-based SHGC with low slag content using micromechanical modelling to provide able guidance for the mixture design. The influencing physical properties of fiber, matrix and interface as input parameters were characterized through intensive experimental processes and the micromechanical model served as a predictive tool for the tensile performance of SHGC. In addition, the feasibility and effectiveness of using micromechanical modelling for the design of SHGC are demonstrated and experimentally verified.

2. Materials and methods

2.1. Materials

The solid precursors used in this study were ground granulated blast furnace slag and Class F fly ash according to ASTM 618 [32] produced locally in the Netherlands. The material density of slag and fly ash are 2890 kg/m³ and 2440 kg/m³, respectively. The d50 particle size for slag is 17.88 μm and 33.19 μm for fly ash. The chemical compositions measured from X-ray fluorescence along with other properties of

precursors (including LOI at 950 °C and fineness passing 45 μm) are shown in Table 1. The fiber used in this study is polyvinyl alcohol (PVA) fiber with 1.2% oiling on the surface, the mechanical and physical properties of which are presented in Table 2.

The crystalline phases were determined using powder X-ray diffraction (XRD). The XRD patterns of slag and fly ash are shown in Fig. 1. The major crystalline phases in fly ash are quartz, mullite and hematite, while the blast furnace slag contains mainly amorphous phases. The only minor crystalline phase of calcite is detected due to possible carbonation. All precursors contain considerable amounts of amorphous phases as can be reflected from the hump in the XRD patterns (from 17° to 35° for fly ash and from 25° to 35° for slag). The reactivity of slag could be indicated by its abundant amorphous content (over 98%). On the other hand, the reactivity of fly ash is reflected by its reactive silica content of 43.04% and reactive alumina content of 15.51%, as reported in a previous study [19]. The same solid precursors have also been used in several previous studies [33–35] and good mechanical properties were achieved.

The alkaline activator was prepared by dissolving solid NaOH pellets (analytical grade, purity≥98%) and liquid sodium silicate (Na₂O: 8.25 wt%, SiO₂: 27.50 wt%) in distilled water. The activator was allowed to cool down to room temperature prior to mixture preparation.

2.2. Micromechanics-guided design

2.2.1. Micromechanics criteria for composite strain-hardening

The pseudo strain-hardening (PSH) criteria used within the micromechanical model by Li and Leung [29] were adopted following a J-integral energy approach suggested by Marshall and Cox [36]. The fundamental requirement for PSH is a steady-state crack opening under tension. To elaborate, an alternative flat crack propagation mode over the oval-shaped Griffith-type crack propagation mode is considered desirable for the PSH to occur. These requirements ensure a sequential initiation and steady-state propagation of matrix micro-cracking, which enables PSH and multiple cracking of SHCC instead of catastrophic failure by formation of one single crack.

To ensure PSH to occur in SHCC reinforced with randomly oriented short cut fibers, the following two criteria have to be met, including a strength-based criterion (Equation (1)) and an energy-based criterion (Equation (2)). Both criteria are schematically illustrated in Fig. 2, which shows the complete fiber bridging stress (σ) versus crack opening (δ).

$$\sigma_{fc} \leq \sigma_0 \tag{1}$$

$$J_{tip} \leq \sigma_0 \delta_0 - \int_0^{\sigma_0} \sigma(\delta) d\delta \equiv J_b' \tag{2}$$

The first criterion is the strength-based criterion for crack initiation (Equation (1)), which requires that the first cracking strength (σ_{fc}) of matrix must not exceed the maximum fiber bridging strength (σ_0). In other words, this ensures that the initiation of a new crack can occur when the tensile stress level does not exceed the fiber bridging capacity.

The second criterion is the energy-based criterion for flat crack propagation (Equation (2)), which requires the crack-tip toughness (J_{tip}) of the composite matrix to be lower than the maximum available complementary energy (J_b'). The J_{tip} represents the energy to break-down the matrix material at the crack tip, which approaches K_{Ic}^2/E_m when the fiber content is small. Here the K_{Ic} and E_m refer to the fracture toughness and elastic modulus of the matrix, respectively. The energy balance during a steady-state (SS) crack propagation is presented as Equation (3), where the work done ($\sigma_{ss}\delta_{ss}$) on the crack body is consumed as the strain energy by fiber bridging and the remaining as the complementary energy for crack tip propagation. Hence, in this case, the complementary energy for SS crack propagation equals to J_{tip}. On the other hand, the J_b' represents the maximum complementary energy considering the upper limit for the fiber bridging, i.e., when the peak

Table 1
Chemical compositions and properties of raw materials.

Oxide (wt %)	SiO_2	Al_2O_3	Fe_2O_3	CaO	MgO	SO_3	Na_2O	K_2O	LOI	Fineness, % passing 45 μm
Slag	32.91	11.84	0.46	40.96	9.23	1.60	–	0.33	1.15	95
Fly ash	52.90	26.96	6.60	4.36	1.50	0.73	0.17	–	3.37	81

Table 2
Physical and mechanical properties of PVA fiber.

Fiber	Diameter (μm)	Density (g/cm3)	Length (mm)	Strength (MPa)	Young's modulus (GPa)
PVA	40	1.30	6–12 (to be selected)	1640	41.1

stress and crack opening reached their maximum value σ_0 and δ_0. Here the J_{tip} and the J_b' are marked as the shaded area and the hatched area in Fig. 2, respectively.

$$\sigma_{ss}\delta_{ss} - \int_0^{\sigma_{ss}} \sigma(\delta)d\delta = J_{tip} \approx \frac{K_{Ic}^2}{E_m} \quad (3)$$

Unsatisfied strength criterion exhausts the fiber bridging capacity of the composite. On the other hand, violation of the energy criterion results in Griffith-type crack propagation. Either violation prevents the composite to exhibit the strain-hardening behavior but rather promote a conventional tension softening behavior.

Considering material variability mainly due to the heterogeneous fiber dispersion as well as the flaw distribution, sufficient margins between σ_{fc} and σ_0, J_{tip} and J_b' have to be maintained for PSH behavior to occur.

Previous studies on SHCC proposed two purely empirical PSH indices for both strength and energy criteria to be used to reflect the margin sizes and thus the possibility of saturated multiple cracking and PSH behavior, namely the strength PSH index (σ_0/σ_{fc}) and the energy PSH index (J_b'/J_{tip}) [38]. Although not quantitatively related in a direct manner, the higher values of these two indices indicate the greater possibility of saturated multiple cracking and PSH behavior and thus better tensile strain capacity of the composite. It has been determined from experimental data that a $\sigma_0/\sigma_{fc} \geq 1.5$ and a $J_b'/J_{tip} \geq 3.0$ are needed for a robust tensile strain-hardening performance [22,24,38,39] of SHCC.

2.2.2. The starting point and matrix design

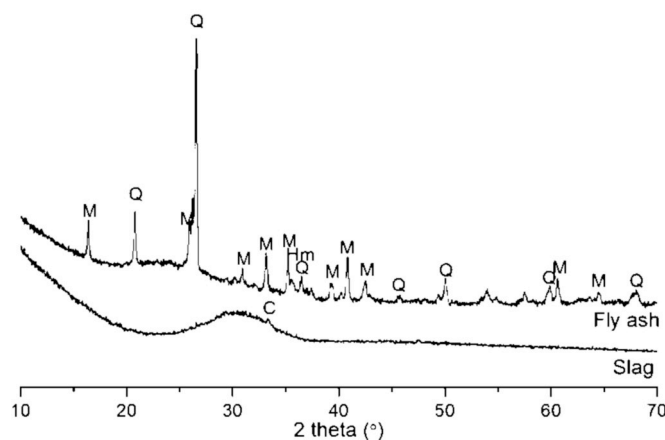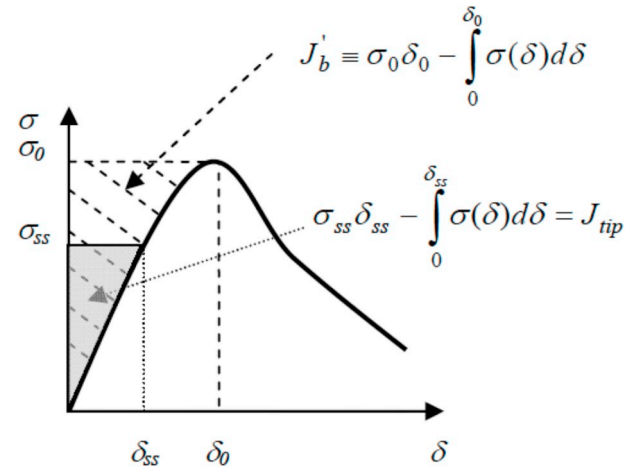The starting point of the matrix design originates from a PVA fiber-

Fig. 2. The representative σ-δ relationship for fiber bridging [37].

reinforced alkali-activated composite that exhibits good deflection-hardening behavior [35]. It has been reported that the microstructure and reaction kinetics of slag (-fly ash) based geopolymer is significantly influenced by the available silica content for geopolymerization reaction. Thus, the silicate modulus (Ms = SiO_2/Na_2O molar ratios) of the alkaline activator plays an important role and strongly determines the mechanical properties of the mixture [40–42]. With regard to compressive strength specifically, there always seems to be an optimum range of activator silicate modulus. One preliminary study of the authors reveals that satisfactory compressive strength was achieved by a slag-fly ash binder with 30 wt% slag and 70 wt% fly ash as solid precursor. Additionally, mixtures with silicate modulus higher than 1.5 tend to yield lower compressive strength [35]. With the assumption that the activator silicate modulus is the main influence factor on mechanical properties for certain precursor combinations, this study has chosen four different moduli (0.8, 1.0, 1.2 and 1.5) and the mixtures were named M0.8, M1.0, M1.2 and M1.5 accordingly. The Na_2O wt.% content with respect to binder mass was kept constant at 4%. The water to binder (w/b) ratios were kept constant at 0.32 to guarantee adequate workability for all mixtures. The detailed matrix design is presented in Table 3.

For matrix mixtures preparation, the solid precursors were first dry-mixed for 5 min at a low speed using a HOBART® mixer. Alkaline activator solution was then added gradually into the mixer and the batches were mixed for an additional 5 min at medium speed. The fresh paste mixtures were cast in polystyrene prism molds ($40 \times 40 \times 160$ mm^3) or cylindrical molds of 55 mm in diameter (D) and 110 mm in length (L). All mixtures were then compacted by vibration

Fig. 1. XRD patterns of solid precursors (Q: quartz, M: mullite, Hm: hematite and C: calcite).

Table 3
Matrix mixture proportions of slag-fly ash geopolymer for SHGC (with respect to total binder mass).

Mixture	Precursor (wt.%)		Alkaline activator (wt.%)		
	Slag	Fly ash	Na_2O	SiO_2	Water
M0.8	30	70	4	3.1	32
M1.0				3.88	
M1.2				4.65	
M1.5				5.8	

and sealed with plastic wrap. The samples were cured in a climate room (20 °C and ≥98% RH) prior to testing.

2.2.3. Micromechanical parameters determination

To implement the micromechanical model, determination of micromechanical parameters regarding matrix (σ_{fc} and J_{tip}) and fiber bridging properties (σ_0 and J_b') are necessary. In this study, σ_{fc} and J_{tip} ($=K_{Ic}^2/E_m$) are directly obtained from tensile splitting tests, fracture toughness and elastic modulus tests, respectively. σ_0 and J_b' are determined from the σ-δ relationship simulated by the micromechanical modelling using experimentally tested data on fiber/matrix interface.

2.2.3.1. Matrix parameters determination.

The splitting tensile strength was measured as the first cracking strength (σ_{fc}) of the matrix in accordance with ASTM, C496 Standard [43]. It should be noted that the splitting tensile tests were conducted using cylindrical specimens with 55 mm in diameter (D) and 110 mm in length (L). The σ_{fc} is calculated following Equation (4):

$$\sigma_{fc} = \frac{2P_{Max}}{\pi LD} \quad (4)$$

where P_{max} [N] is the maximum load during splitting, L [mm] and D [mm] are the length and diameter of the specimen, respectively.

The fracture toughness (K_{Ic}) and elastic modulus (E_m) at 28 days were experimentally obtained. The E_m were measured using prism samples according to ASTM C469 [44]. The K_{Ic} were determined using single-edge notched specimens with 40 mm in depth (W), 40 mm in width (B) and 160 mm in length. The single-edge notches with 1.5 mm in width, 40 mm in length and 12 mm in notch depth (a) were prepared using a diamond cutting saw prior to testing. The relative notch depth ratio α ($\alpha = a/W$) was kept to be 0.3, which is considered to be practical to conduct experiments under the current test configuration. The three-point bending (3 PB) tests were performed on a closed-loop INS-TRON machine with the crack mouth opening displacement (CMOD) rate of 0.01 mm/min. The CMOD was controlled using two LVDTs, which were attached to the two sides of the preformed notch on the side surfaces of the prism. The prism was supported over a load span (S) of 120 mm. The detailed testing set-up is shown in Fig. 3. At least 6 specimens were tested for each mixture.

Assuming linear elastic fracture mechanics (LEFM) holds for the fine grain matrix material (without fiber), K_{Ic} is computed from Equation (5) using the peak load P_{Max} [N] from the 3 PB test, as has been widely used in previous studies and recommendations [22,45–47].

where B is the specimen width [mm], W is the specimen depth [mm], S is the loading span [mm], a is the notch depth and $\alpha = a/W$ (0.3) is the relative notch depth ratio. Additionally, the compressive strength of matrix specimens cured for 28 days was measured in accordance with NEN 196-1 standard [48].

2.2.3.2. Interface parameters determination.

The interface properties were determined using single fiber pullout tests following previous studies by Redon et al. [49]. A micro tension-compression testing device (Kammrath & Weiss) was used as shown in Fig. 4. Both the surface of the thin specimen and the free end of the PVA fibers were glued to two small metal blocks. Afterwards, they were mounted on the testing device using two metal blocks, which were fixed to an actuator and a load cell. A 10 lb (44.48 N) load cell was included in the system for pullout load testing with an accuracy of 0.1%. Displacement-controlled pullout was conducted with a constant displacement rate of 0.01 mm/s to avoid fiber rupture while revealing reliable information of the frictional force. At least 20 tests were conducted for each fiber/matrix combination. More details of this experimental set-up can be found in Ref. [34].

To quantitatively determine the interface properties, at least three interface characteristics including chemical bond G_d, frictional bond τ_0, and slip-hardening coefficient β, were derived from the single fiber pullout curves according to Equations (6)–(8) [49].

$$G_d = \frac{2(P_a - P_b)^2}{\pi^2 E_f d_f^3} \quad (6)$$

$$\tau_0 = \frac{P_b}{\pi d_f L_e} \quad (7)$$

$$\beta = \frac{d_f}{L_e}\left(\frac{(\Delta P/\Delta S|\Delta S\to 0)}{\pi \tau_0 d_f} + 1\right) \quad (8)$$

where E_f, d_f and L_e are the elastic modulus, diameter and embedded length of PVA fiber respectively. $\Delta P/\Delta S$ is the initial slope of the pullout load vs displacement. P_a is the load up to full debonded length (debonded length L_d = embedded length L_e) and P_b is the load when the fiber begins to slip.

2.2.4. Micromechanical modelling

Micromechanical modelling based on fracture mechanics provides an opportunity of tailoring micro-parameters and thus modification of the failure mode, the tensile strength, and ultimate tensile strain of composite material [50]. In this study, the micromechanical modelling was performed using a modified fiber bridging constitutive law devel-

$$K_{Ic} = \frac{1.5\,P_{Max}\,S\sqrt{\pi a}}{B\,W^2}\left(\frac{0.68 - 0.744\alpha}{1 - 2.155\alpha + 1.161\alpha^2} + 0.36 - 2.088\alpha + 4.611\alpha^2 - 6.499\alpha^3 + 4.232\alpha^4\right) \quad (5)$$
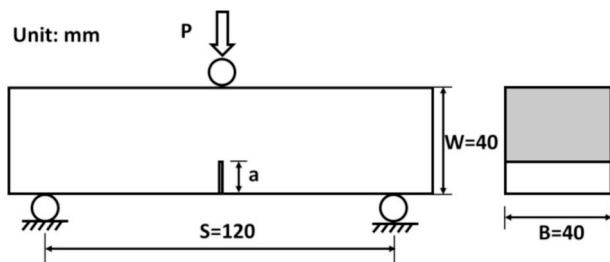

Fig. 3. Three-point bending test configuration for single-edge notched prism specimen.

oped by Yang et al. [51]. The model links the single fiber/matrix interaction to the fiber bridging behavior of a single crack (σ–δ relationship), and the simulated results are used to evaluate the potential for PSH of composite material as described in Section 2.2.1. The most important simulated results from the model are the σ-δ relationships of single fiber bridging. Although the matrix micro-spalling [52] and the Cook-Gordon effect [53] were not taken into consideration for brevity, the two-way pullout mechanism was considered here to improve the accuracy of crack opening prediction [39]. Given the dimension of samples, the fiber distribution within geopolymer matrix was considered to be two-dimensional. The apparent strength [54], snubbing coefficient [54] and strength reduction factor [55] of PVA fiber was assumed to be the same as in previous studies, which have been estimated
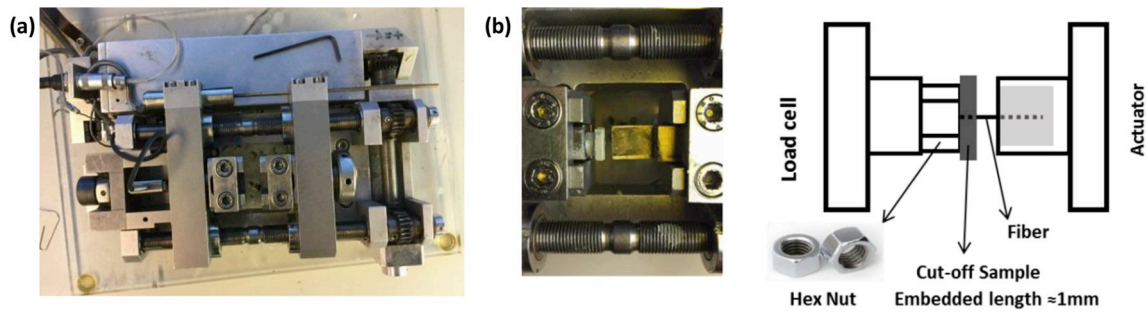
Fig. 4. Single fiber pullout test: (a) Micro tension-compression device, (b) photo and schematic tests set-up.

experimentally in cementitious systems and used in previous SHGC design [22]. The experimentally tested micromechanical parameters of matrix and interface presented in Section 3.1 served as modelling input. The simulation results from micromechanical modelling could guide the required selection or modification of the micromechanical parameters to achieve the desired strain-hardening performance of SHGC.

The micromechanical modelling in this study was conducted for two purposes. On one hand, the knowledge on simulated results aids the selection of fiber length (L_f) and fiber volume (V_f) for an optimal composite design. On the other hand, it serves as a prediction tool for the final tensile performance of selected mixtures to guide the SHGC development.

2.3. Tensile performance verification

The tensile performance of four composite mixtures following the guidance of micromechanics-based composite design was evaluated by uniaxial tensile tests, which served as verification for the effectiveness of the micromechanics-guided design approach. Specifically, the test seeks to confirm if the most promising composite mixture suggested by the micromechanical modelling could exhibit significant strain-hardening behavior with high tensile ductility over 3%, which is considered comparable to SHCC materials. The matrix mixtures were firstly prepared and the PVA fiber was slowly added. The fresh composite mixtures were then cast into dogbone-shaped molds and were sealed after compact vibration. All composite mixtures were cured under identical conditions as matrix mixtures for 28 days before mechanical testing.

Uniaxial tensile tests were conducted using dog-bone shaped composite samples recommended by the Japan Society of Civil Engineers [56], which is shown in Fig. 5 (b). Dog-bone samples with a testing volume of $13 \times 80 \times 30\,mm^3$ were clamped using two pairs of steel plates, which were tightened with bolts. Four Al plates were glued on both sides of the specimen 1 day prior to clamping to improve the frictional force. Two LVDTs were mounted on both sides of the specimen. Following RILEM recommendation [57], this set-up includes both rotationally fixed ends. The tests were conducted using displacement control by LVDTs at a rate of 0.01 mm/s. At least 4 samples were tested for each composite mixture.

3. Results and discussions

3.1. Micromechanical parameters

3.1.1. Matrix properties

The mechanical properties of the matrices determined by various experiments are summarized in Table 4. The splitting tensile strength (f_{st}) is tested according to the modified ASTM C496 standard [43] in this study as the first cracking strength σ_{fc} instead of uniaxial tensile strength for greater data stability.

With increasing activator silicate modulus (M0.8–1.5), the compressive strength (f_c) and elastic modulus (E_m) are evidently influenced and the trend of which agrees well with each other. Both properties first increase with the increase of silicate modulus and then decline after reaching a maximum value at the modulus of 1.2. This
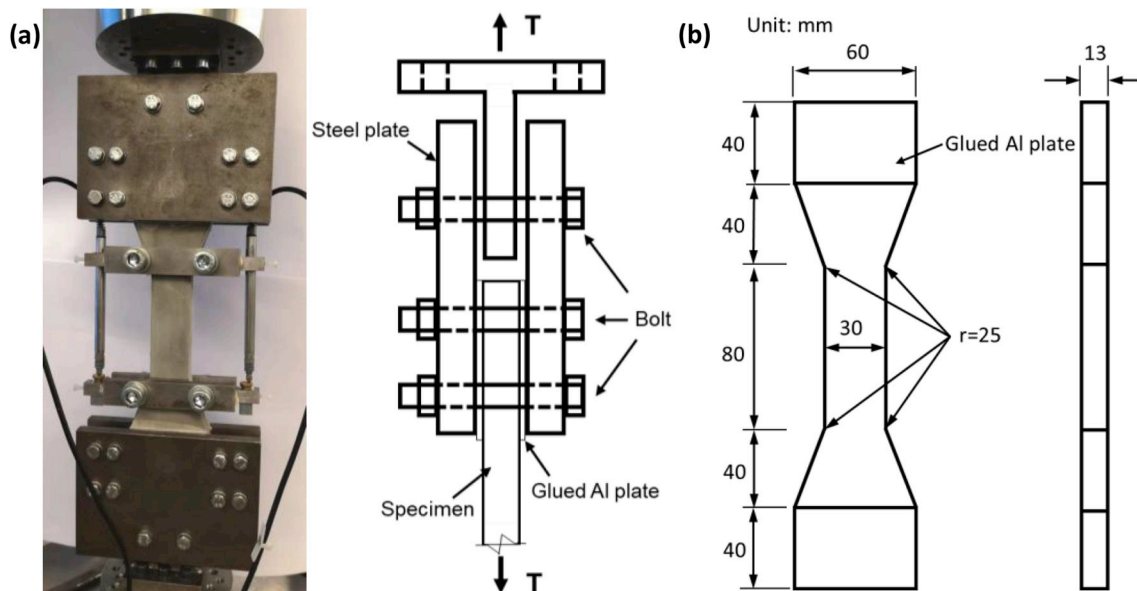

Fig. 5. Uniaxial tensile test: (a) Experimental set-up and (b) dimensions of dog-bone shaped samples.

Table 4
Matrix properties as input parameters for the micromechanical model.

Matrix	Compressive strength f_c (MPa)	Splitting tensile strength f_{st} (MPa)	Elastic Modulus E_m (GPa)	Fracture toughness K_{Ic} (MPa)	Crack tip toughness J_{tip} (J/m^2)
M0.8	57.3 ± 1.1	2.9 ± 0.34	11.9 ± 0.33	0.229 ± 0.011	4.46 ± 0.45
M1.0	59.6 ± 1.1	2.4 ± 0.27	12.4 ± 0.35	0.241 ± 0.009	4.70 ± 0.37
M1.2	62.3 ± 1.2	2.0 ± 0.19	13.0 ± 0.30	0.194 ± 0.007	2.89 ± 0.21
M1.5	54.4 ± 0.7	2.8 ± 0.47	9.2 ± 0.53	0.153 ± 0.004	2.54 ± 0.15

influence of activator silicate modulus has been confirmed by a previous study on slag/fly ash-based geopolymer pastes/mortars [58]. The fracture properties, including fracture toughness (K_{Ic}) and crack tip toughness (J_{tip}) are found to first increase from silicate modulus of 0.8–1.0 and then decrease with higher silicate modulus. The highest value of K_{Ic} reaches 0.241 J/m^2 at the silicate modulus of 1.0. Furthermore, it could be observed that the influence of silicate modulus on K_{Ic} follows a different trend compared to that of compressive strength and elastic modulus. According to the authors, this disagreement might indicate that the microstructure and reaction products also largely influence the fracture behavior of slag/fly ash-based geopolymer matrix [46,59]. The results of mechanical properties suggest that geopolymer matrix is very sensitive to alkaline activation conditions. In this case, changing the silicate modulus from 1.0 to 1.2 might result in differences in the amount of reaction products and/or in the chemical nature of reaction products, which consequently leads to different fracture properties [59].

3.1.2. Fiber/matrix interface properties

Due to the hydrophilic properties to hydrates, PVA fiber presents special interface features compared with other synthetic fibers, which is characterized by its chemical bonding (G_d), initial fictional bonding (τ_0) and slip-hardening coefficient (β) [49]. As has been described in Section 2.2.3, these interface properties were quantitatively determined using single fiber pullout tests and are summarized in Table 5. With the increment of activator silicate modulus, the development of G_d and β coincide well with each other. Their values first increase and then decrease after reaching the maximum at modulus of 1.0. Interestingly, G_d shows identical trends as K_{Ic} and J_{tip} as a function of activator silicate modulus. As has been discussed in Section 3.1.1, this might serve as evidence that chemical bonding is also closely related to the microstructure and reaction products. The main reaction products were characterized in identical systems as C-(N)-A-S-H type gel [59]. By increasing the silicate modulus of alkaline activator, more available silica species were introduced into the matrix and consequently changed the global reaction and chemical nature of the reaction products [41,60,61]. Thus, the adhesion properties of PVA fiber/matrix changed accordingly, which was reflected by the variation of G_d in a range from 1.57 to 3.20 J/m^2.

Unlike G_d which is predominantly related to chemical adhesion properties, τ_0 and β on the other hand, are more physically related to the friction during pullout processes. As shown in Table 5, it is found that τ_0 follows a different trend than G_d, reaching a maximum value at modulus of 1.2. On the other hand, β shows a similar trend as G_d (K_{Ic} and J_{tip}) with the increase of silicate modulus. This inconsistency between τ_0 and β could be due to the different mechanisms behind. τ_0, following

coulomb-type friction law, is determined by the fiber-matrix friction coefficient and the shrinkage-induced residual normal stress of matrix onto the fiber surface [62,63]. While for β, fiber abrasion between fiber surface and matrix during the pullout process can instigate a so-called 'jamming' effect due to the accumulation of stripped fibrils on the fiber surface [64]. This effect tends to be more severe when the fracture surface roughness of the matrix is higher. As has been previously reported, the fracture surface roughness is positively related to the matrix fracture toughness (K_{Ic}) [65]. Consequently, the trend of β with increasing activator silicate modulus in this study agrees well with K_{Ic} in Table 4. Although previous studies reported that the trend of τ_0 is also consistent with K_{Ic} [25], it is not found in this study. Since the normal force also plays a significant role in determining friction, this inconsistency could be due to the synergistic effect of surface fracture roughness (in line with K_{Ic}) and shrinkage-induced normal stress.

It is worth noting that the average value of G_d in SHGC matrix is in general 1.5 to 2.5 times higher than that in conventional SHCC [62]. In addition, the average τ_0 is also found to be about 2–3 times higher [7, 62]. On the other hand, the average β for SHGC is much lower compared to those in SHCC, which typically lies between 0.58 and 0.63 [51]. These findings are in line with several previous studies of SHGC [22,66] and thus demonstrate significant differences in interface properties of SHGC. It is believed that this difference is at least partially due to the differences in the chemical composition of the reaction products, as has already been discussed previously in this section and Section 3.1.1. Further experimental studies on the influence of SHGC microstructure and reaction products near the interface are needed for further clarification of these differences.

3.2. Selection of fiber volume and fiber length

It is well acknowledged that fiber properties play significant roles in the performance of fiber-reinforced composite. Among those, fiber volume (V_f) and fiber length (L_f) are the two most convenient ones to be adjusted in comparison to the modification of fiber surface characteristics. Therefore, as a first step, the micromechanical model was used to aid in the selection of L_f and V_f for an optimal composite design. To this end, the critical fiber volume (V_f^{crit}) as a function of L_f for saturated strain-hardening was determined by inputting all micromechanical parameters (Tables 4 and 5) into the micromechanical model and taking into account of the two strain-hardening criteria. More specifically, by changing V_f^{crit} for each L_f, the V_f^{crit} vs L_f curve is inversely fitted to meet the two PSH index requirements, i.e., the strength PSH (σ_0/σ_{fc}) ≥ 1.5 and the energy PSH (J_b'/J_{tip}) ≥ 3.

The calculated curves for V_f^{crit} as a function of L_f for M0.8–1.5 are shown in Fig. 6(a)-(d). All curves for V_f^{crit} vs L_f concave upwards while decreasing. As illustrated in all four figures, increasing L_f leads to lower V_f^{crit} indicating that longer L_f is more effective to achieve strain-hardening.

In order to choose V_f and L_f for potential strain-hardening, the overlapping area above both curves is considered (meeting both criteria (1) and (2)) and is shown in Fig. 6 (e). The goal here is to adopt a minimum fiber content to achieve saturated strain-hardening and multiple cracking. Although larger L_f proves to be more effective, it is recognized that longer fiber length also negatively influences mixture workability and hinders proper fiber dispersion inside the matrix. Thus, the limits of V_f up to 3% and L_f up to 12 mm are set as boundary

Table 5
PVA fiber-matrix interface properties as input parameters for the micromechanical model.

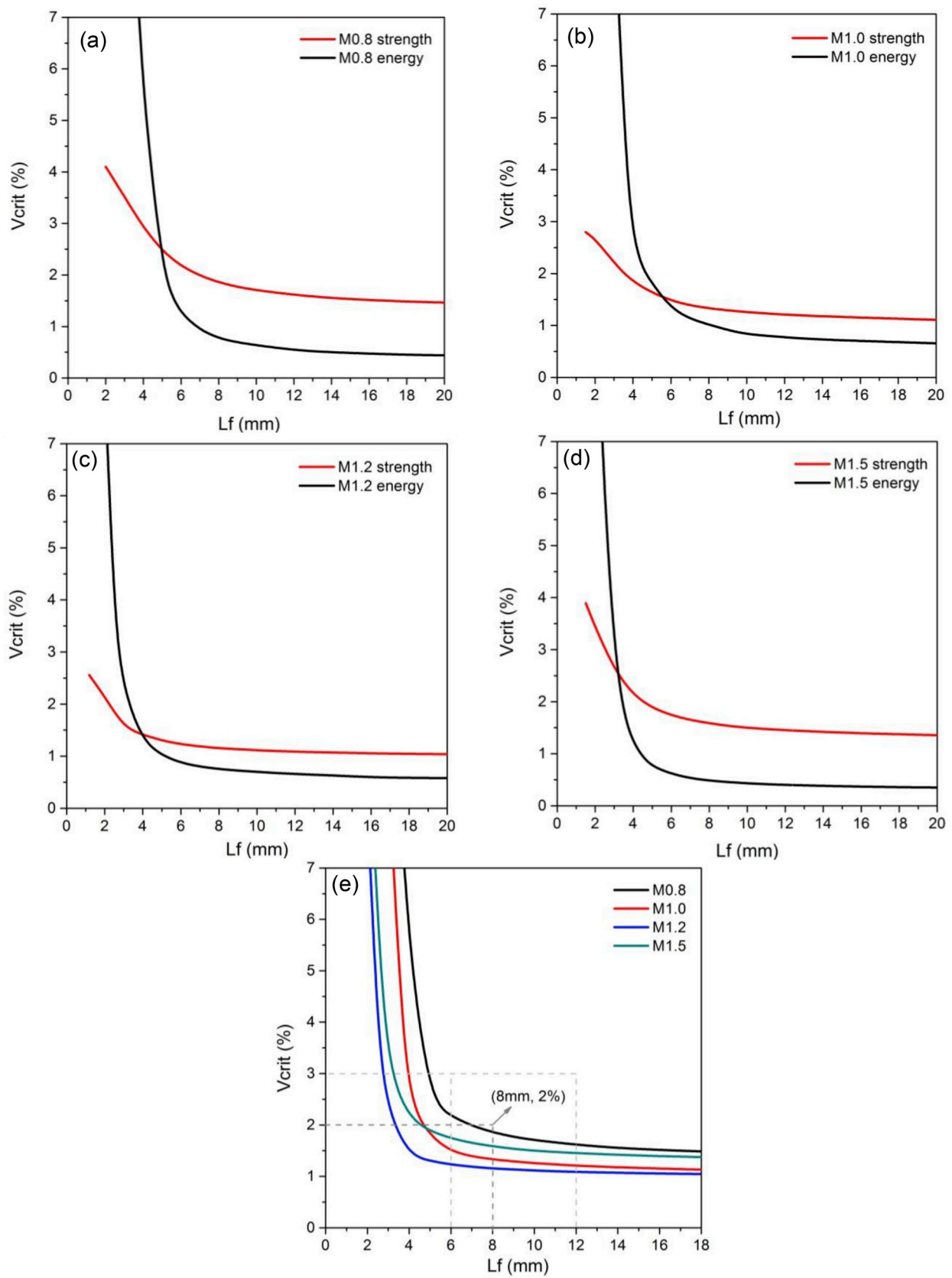| Interface	Chemical bonding energy G_d (J/m^2)	Frictional bond τ_0 (MPa)	Slip-hardening coefficient β	Snubbing coefficient	Strength reduction coefficient
M0.8	1.57 ± 0.84	1.81 ± 0.78	0.33 ± 0.11	0.2	0.33
M1.0	3.20 ± 1.26	2.80 ± 0.76	0.39 ± 0.12		
M1.2	2.86 ± 1.08	4.01 ± 1.16	0.26 ± 0.09		
M1.5	2.53 ± 1.04	3.13 ± 1.10	0.25 ± 0.06		

Fig. 6. V_f^{crit} as a function of L_f determined by both energy and the strength criterion (a)M0.8, (b)M1.0, (c)M1.2, (d)M1.5, and the combined effect of both energy and strength criteria (e)M0.8-M1.5.

conditions. In the end, a V_f of 2% and L_f of 8 mm were selected for further studies. The corresponding point of (L_f, V_f) is also marked in Fig. 6 (e). This point meets both strain-hardening criteria for all four mixes studied.

It is observed that the point corresponds to selected V_f and L_f (8 mm, 2%) is furthest away from the V_f^{crit} vs L_f curves of M1.2, suggesting that this mix could be the most promising for strain-hardening. This observation will be further substantiated in the following section. Furthermore, it is important to note that the V_f and L_f chosen this way might not be optimal for each of the investigated mixtures to achieve saturated strain-hardening with minimum fiber addition. However, for later tensile performance verification and comparison purposes, this study chose this V_f and L_f combination for all composites. This micromechanics-guided mixture design of SHGC is shown in Table 6, and was further evaluated by micromechanical modelling and the tensile performance of which are experimentally verified in the follow-up section.

3.3. Micromechanical modelling of stress vs crack opening relationships

Micromechanical modelling was employed to compute the σ-δ relationships as described in Section 2.2.4, in order to predict the tensile performance of the four SHGC mixtures listed in Table 6. The simulated σ-δ curves are illustrated in Fig. 7 (a). As can be seen, σ-δ relationships for SHGC mixture M0.8–1.5 show clear differences. The fiber/matrix interface properties play crucial roles here for crack bridging behavior and thus determine the shape of the σ-δ curves. At least three characteristics of σ-δ curves dominated by different interface properties could be observed. The magnitude of the y-intercept is positively related to G_d, which indicates that a certain load is needed to destroy the chemical bonding. As fiber length, diameter and volume content are already selected, the peak bridging stress is largely governed by $τ_0$ [55]. In addition, β influences the shape second peak/peak shoulder (if any), which corresponds to the post fiber pullout process during crack bridging. As mentioned previously in this work, several output parameters could be obtained from the σ-δ relationships. Accordingly, the predicted peak bridging stress ($σ_0$), the corresponding crack opening ($δ_0$) and the complementary energy (J_b') are listed in Table 7. Compared to conventional SHCC, G_d obtained in this study are typically higher and thereby could result in smaller crack width by suppressing the crack opening during the strain-hardening stage [22]. Besides, while a relatively lower β might lead to lower peak bridging capacity $σ_0$, the relatively higher $τ_0$ is actually beneficial for yielding a higher $σ_0$ and J_b'. Hence, as long as both criteria are met, a high tensile strain capacity could still be achieved.

To assess the potential of SHGC to achieve strain-hardening and multiple cracking, two PSH indices, i.e., energy PSH index (J_b'/J_{tip}) and strength PSH index ($σ_0/σ_{fc}$), were calculated using experimentally-attained input matrix and interface properties, and the micromechanical modelling output (i.e., J_b' and $σ_0$). The results of both PSH indices for all designed SHGC are summarized in Fig. 7 (b). This study followed previous research concerning conventional SHCC, which proposed two empirical values for two PSH indices: 1.5 for strength PSH index and 3 for energy PSH index [22,24,38,39]. As illustrated in Fig. 7 (b), both PSH indices are greater than those suggested for all the

mixtures, which indicates that both the strength and energy-based criteria are well met. Therefore, according to the prediction by micromechanical modelling, all designed mixtures could exhibit tensile strain-hardening behavior with multiple cracking. Particularly among others, M1.2 reveals both high energy and strength PSH indices. On the contrary, M0.8 and M1.5 only have high energy PSH indices while the strength PSH indices are comparably lower than the others. M1.0, on the other hand, has a high strength PSH index (2.3) while its energy PSH index (5.7) is the lowest among all mixtures. Consequently, M1.2 according to the prediction is considered optimal with the highest potential for tensile strain-hardening and multiple cracking behavior.

3.4. Uniaxial tensile performance verification of designed mixtures

Experimental verification was performed to evaluate the effectiveness and accuracy of the prediction by micromechanics-guided design approach. The uniaxial tensile performance of the proposed SHGC M0.8–1.5 is shown in Fig. 8. The tensile test results characterized by first cracking tensile strength ($σ_{fc}$), ultimate tensile strength ($σ_{ult}$), tensile strain capacity (ε) and average crack width are presented in Table 8. It is found that all SHGC mixtures exhibit evident strain-hardening behavior although the tensile strain capacity varies largely. $σ_{fc}$ is obtained by taking the stress value at the moment when the first crack initiates. Compared to the tensile splitting strength (f_{st}) of the SHGC matrices presented in Table 4, $σ_{fc}$ is found to be a bit higher than f_{st} of the plain matrix, which is due to the enhanced role of fiber bridging on the composite first crack strength [67]. This observation also agrees well with the fact that $σ_{fc}$ is comparably higher than the matrix uniaxial tensile strength, which was reported in previous research of SHGC [22]. Additionally, it is found that with increasing activator silicate modulus used to prepare SHGC, the trend of $σ_{fc}$ is in good agreement with that of f_{st}. This correlation is reasonable and also confirms the feasibility of using f_{st} instead of $σ_{fc}$ as input for the micromechanical model.

Additionally, all SHGCs exhibited moderate ultimate tensile strength $σ_{ult}$ in the range of 3.4–4.4 MPa. Theoretically, $σ_{ult}$ should be equal to simulated peak bridging stress $σ_0$. However, the $σ_{ult}$ from uniaxial tensile tests compared to $σ_0$ is found to be considerably lower. Moreover, inconsistency between $σ_{ult}$ and $τ_0$ as shown in Table 5 is found in this study, which does not agree with the trend of $σ_0$ in simulation results. These discrepancies could be attributed to the simplified assumption made when computing the σ-δ relations. The micromechanical model considers the fibers to be in a perfect state of random distribution within the matrix. In the experiments, however, the actual fiber dispersion is influenced by the processing details and may be expected to deviate from a perfectly random dispersion. As $σ_0$ is governed by the weakest section with the lowest fiber content, these differences between simulated and experimental results are unavoidable. In fact, this is also the reason that M1.2 does not show the highest $σ_{ult}$ as predicted in Table 7. Similar findings on those discrepancies were reported in previous studies concerning both SHCC [68] and SHGC [23] system.

As for tensile ductility, moderate to high tensile strain capacity are found within the range of 2.3%–4.8%. As predicted, M1.2 shows promising strain-hardening behavior with the highest tensile ductility up to 4.8%. It is worth noting that although M1.5 yields lowest tensile ductility (2.3%), this tensile strain capacity is already several hundred times that of conventional concrete. Additionally, the average crack width was also estimated using the actual elongation calculated from the tensile strain capacity and the number of visible cracks on the sample surface. As listed in Table 8, the crack widths of SHGC are within a range of 28.4–84.2 μm. However, it seems that the experimentally obtained average crack width is not consistent with the predicted crack width in Table 7. According to Li et al. [69], the actual loaded crack width should be smaller than the experimentally estimated values, because the actual number of micro-cracks developed during loading of the coupon specimen was more than the number of visible cracks on the surface of the unloaded specimen. This discrepancy is further discussed in Section 3.5.

Table 6
Composite mixture design of slag/fly ash-based SHGC.

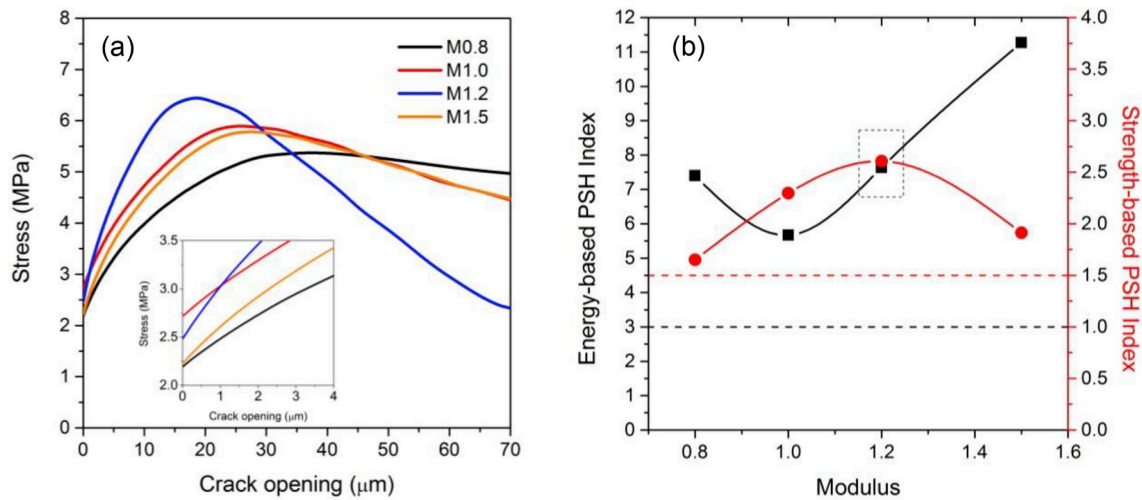| Mixture	Precursor		Fiber		Alkaline activator		
	Slag (wt. %)	Fly ash (wt.%)	V_f (vol %)	L_f (mm)	Na_2O (wt.%)	SiO_2 (wt.%)	Water (wt.%)
M0.8	30	70	2	8	4	3.1	32
M1.0						3.88	
M1.2						4.65	
M1.5						5.8	

Fig. 7. (a) Simulated σ-δ relationship for PVA SHGC; (b) PSH indices as function of activator silicate modulus.

Table 7
Predicted peak bridging stress.

Predicted properties	M0.8	M1.0	M1.2	M1.5
Peak bridging stress σ_0 (MPa)	5.4	5.9	6.5	5.8
Complementary energy J_b' (J/m^2)	32.8	27.5	22.5	28.4
Crack opening δ_0 (μm)	35.5	23.8	18.9	26.5

The obtained results by the uniaxial tensile test verification confirm that the most promising SHGC designed following micromechanics guidance could exhibit significant strain-hardening behavior with high tensile ductility of 4.8% and ultimate tensile strength of 3.8 MPa. Actually, three of the designed SHGC fulfill the requirements of a tensile ductility over 3% and ultimate tensile strength over 3 MPa, which is considered comparable to conventional SHCC with moderate strain-hardening performance. Thus, the slag/fly ash-based SHGC being comparable or even outperforming certain SHCC materials was successfully developed in this study with the aid of micromechanical modelling. It is believed that the developed SHGC constituents of cement-free matrix could primarily enhance the sustainability of the material by simultaneously reducing the embodied energy and CO_2 footprint [22,25,70]. Besides, the experimental verification also served another purpose: to check the reliability of using the average value of micromechanical parameters as model input. Due to limitations by the testing techniques and inhomogeneity induced by processing, some of the input parameters, especially those with regard to interface properties, have relatively large standard deviations. However, the experimental verification confirms that the average values of these properties are considered adequate to be used as input data for the micromechanics-guided design of SHGC.

3.5. Discussion on using micromechanics-guided approach for SHGC design

The development of SHGC compared to that of SHCC is evidently more complicated because many more parameters have to be considered particularly regarding the matrix and interface. These parameters could be related to the chemistry of alkaline activator (Na$_2$O%, silicate modulus, water content) [40–42], the chemical/physical properties of solid precursors [15,58], but also temperature and humidity related curing regime [71–73]. Up till now, due to these complications, the systematic approach of geopolymer concrete design is still not yet developed. Thereby, it further adds to the difficulties when it comes to the design of SHGC. Furthermore, as a novel material recently gaining increasing attention, the available literature with regard to the development of SHGC is still limited. Considering the different origins of solid

precursors and large variances in their chemical/physical properties, it seems that the design of SHGC can only work on a case by case basis. With already existing difficulties related to tensile performance testing of SHGC, the development of SHGC using traditional trial-and-error method would be even more time consuming and largely depend on the very specific circumstances rather than comprehensive scientific knowledge. The micromechanics-guided design approach in this study, on the other hand, is demonstrated to be more effective and practical for SHGC system. The mechanical properties and tensile ductility of proposed SHGC mixtures could be adequately predicted, offering able guidance for composite mixture design while avoiding a large number of tests.

As for the implementation of the micromechanical model, it is worth noting that the values for both energy and strength PSH indices in this study were harvested from the purely empirical values from conventional SHCC. It is observed that these values seem to be compatible with SHGC systems. However, further study is still needed to find more accurate/suitable values for SHGC systems based on different solid precursors. Certain discrepancies do exist with regard to the predictive properties, including the ultimate cracking strength and crack width, which is mainly due to differences between ideal and realistic fiber dispersion. However, the trend for predictive tensile strain capacity is considered satisfactory and could thereby offer useful guidance towards optimal tensile performance in the design process of SHGC.

Finally, it is worth mentioning that the optimal SHGC mixtures, for instance, M1.0 and M1.2, still have room for improvement with regard to their mechanical properties, i.e., first and ultimate cracking strength. Future studies will focus on the enhancement of their mechanical properties while maintaining satisfactory tensile ductility.

4. Conclusions

This study successfully developed several sustainable slag/fly ash-based strain-hardening geopolymer composite (SHGC) with low slag content. The optimal mixtures showed excellent strain-hardening and multiple cracking performances following the guidance from micromechanical modelling. Based on the results and discussions of this study, the following conclusions can be drawn:

- The optimal SHGC mixture M1.2 based 30 wt% slag, 70 wt% fly ash activated by sodium-based silicate solution in this study exhibits promising tensile strain capacity up to 4.8% and ultimate tensile strength of 3.8 MPa, which is considered satisfactory compared to that of conventional SHCC materials.
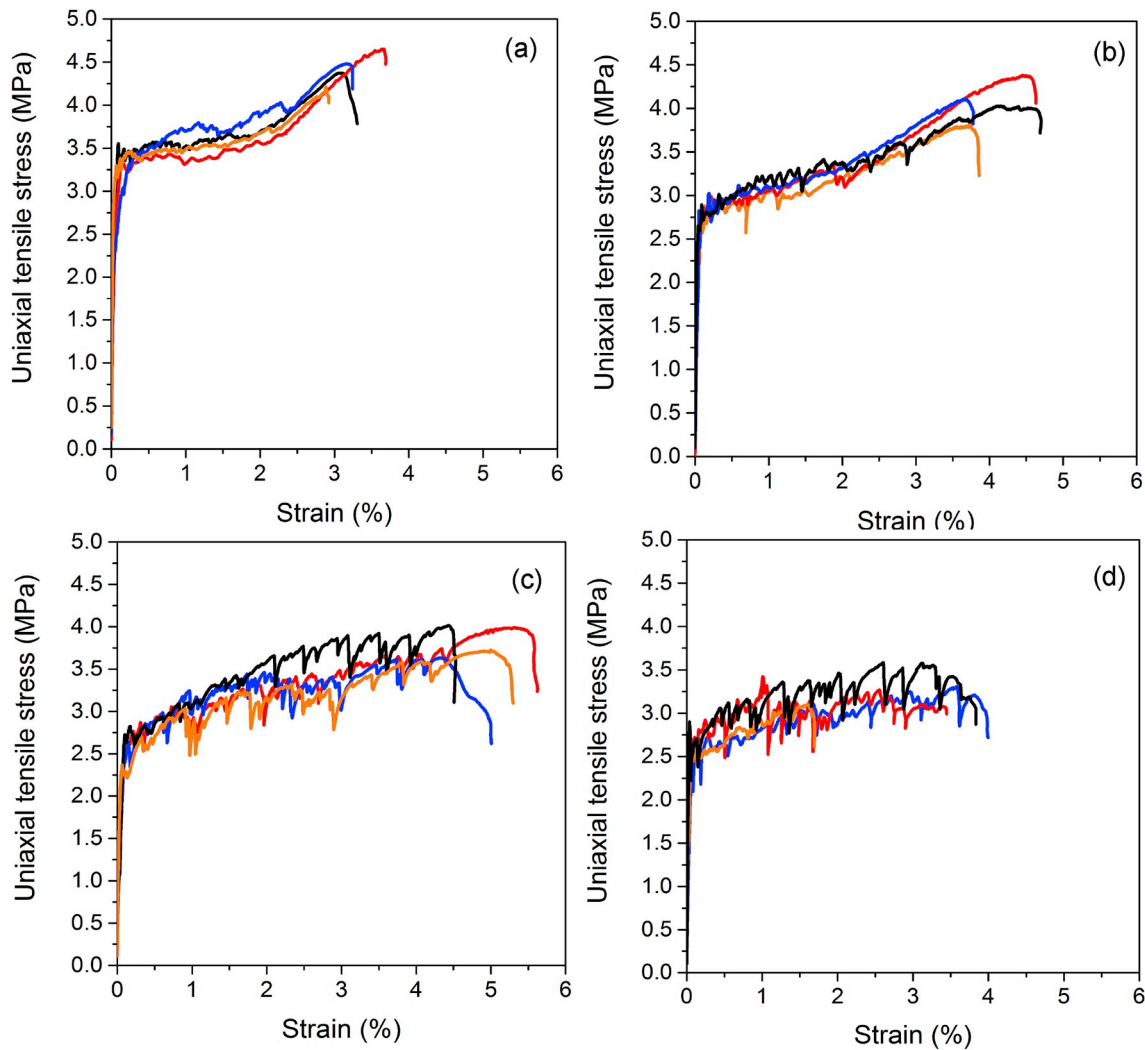
Fig. 8. Uniaxial tensile stress-strain curves of SHGC: (a) M0.8, (b) M1.0, (c) M1.2 and (d) M1.5.

Table 8
The tensile performance of designed SHGC.

Mixture	First cracking strength σ_{fc} (MPa)	Ultimate tensile strength σ_{ult} (MPa)	Uniaxial tensile strain ε (%)	Average crack width (μm)
M0.8	3.4 ± 0.12	4.4 ± 0.19	3.2 ± 0.32	28.4
M1.0	2.8 ± 0.08	4.2 ± 0.18	4.0 ± 0.38	58.4
M1.2	2.6 ± 0.16	3.8 ± 0.19	4.8 ± 0.46	84.2
M1.5	2.7 ± 0.15	3.4 ± 0.21	2.3 ± 1.22	61.0

- The silicate modulus of alkaline activator directly influences the matrix and interface properties and the final strain-hardening properties of SHGC. This study confirms that for a mixture with a given slag/fly ash ratio, changing activator silicate modulus is an efficient approach for modification of the strain-hardening performance of SHGC.
- The consistency of increasing chemical bonding G_d and fracture toughness K_{Ic} with increasing activator silicate modulus serves as evidence that the matrix and interface properties predominantly relate to the chemical nature of the reaction products. On the other hand, the frictional bond and slip-hardening coefficient are more physically related to the fiber/matrix interaction. Particularly, the slip-hardening coefficient β affected by the fracture surface roughness of the matrix correlates well with the matrix fracture toughness K_{Ic}.
- Compared to conventional SHCC, SHGC demonstrates significant differences in interface properties including a stronger chemical bond and frictional bond but a lower slip-hardening coefficient, which, according to the micromechanical model, could lead to higher bridging stress and small crack opening.
- The empirical values of energy and strength PSH indices derived from conventional SHCC are observed to be valid for SHGC as well.
- The micromechanical model linking micromechanical and composite properties serves as an effective tool for the development of SHGC by assisting in the selection of suitable fiber properties, predicting the potential tensile performance and offering guidance for formulating tailoring strategy.

Acknowledgement

References

[1] V.C. Li, On engineered cementitious composites (ECC), J. Adv. Concr. Technol. 1 (3) (2003) 215–230.

[2] V.C. Li, H.-C. Wu, Conditions for pseudo strain-hardening in fiber reinforced brittle matrix composites, Appl. Mech. Rev. 45 (8) (1992) 390–398.

[3] M. Li, Multi-scale Design for Durable Repair of Concrete Structures, The University of Michigan, 2009.

[4] J. Zhou, Performance of Engineered Cementitious Composites for Concrete Repairs, TU Delft, Delft University of Technology, 2011.

[5] J. Zhou, S. Qian, M.G. Sierra Beltran, G. Ye, K. van Breugel, V.C. Li, Development of engineered cementitious composites with limestone powder and blast furnace slag, Mater. Struct. 43 (6) (2010) 803–814.

[6] S. Wang, V.C. Li, Engineered cementitious composites with high-volume fly ash, ACI Mater. J. Am. Concr. Inst. 104 (3) (2007) 233–241.

[7] E.-H. Yang, Y. Yang, V.C. Li, Use of high volumes of fly ash to improve ECC mechanical properties and material greenness, ACI Mater. J. 104 (6) (2007) 620–628.

[8] J. Davidovits, Geopolymers, J. Therm. Anal. Calorim. 37 (8) (1991) 1633–1656.

[9] C. Shi, D. Roy, P. Krivenko, Alkali-activated Cements and Concretes, CRC press, 2006.

[10] J.L. Provis, S.A. Bernal, Geopolymers and related alkali-activated materials, Annu. Rev. Mater. Res. 44 (2014) 299–327.

[11] G. Habert, C. Ouellet-Plamondon, Recent update on the environmental impact of geopolymers, RILEM Tech. Lett. 1 (2016) 17–23.

[12] A. Passuello, E.D. Rodríguez, E. Hirt, M. Longhi, S.A. Bernal, J.L. Provis, A. P. Kirchheim, Evaluation of the potential improvement in the environmental footprint of geopolymers using waste-derived activators, J. Clean. Prod. 166 (2017) 680–689.

[13] J. Van Deventer, J. Provis, P. Duxson, G. Lukey, Reaction mechanisms in the geopolymeric conversion of inorganic waste to useful products, J. Hazard Mater. 139 (3) (2007) 506–513.

[14] P. Duxson, J.L. Provis, G.C. Lukey, J.S.J. van Deventer, The role of inorganic polymer technology in the development of 'green concrete', Cement Concr. Res. 37 (12) (2007) 1590–1597.

[15] I. Ismail, S.A. Bernal, J.L. Provis, R. San Nicolas, S. Hamdan, J.S. van Deventer, Modification of phase evolution in alkali-activated blast furnace slag by the incorporation of fly ash, Cement Concr. Compos. 45 (2014) 125–135.

[16] F. Puertas, A. Fernández-Jiménez, Mineralogical and microstructural characterisation of alkali-activated fly ash/slag pastes, Cement Concr. Compos. 25 (3) (2003) 287–292.

[17] N.K. Lee, H.K. Lee, Reactivity and reaction products of alkali-activated, fly ash/slag paste, Constr. Build. Mater. 81 (2015) 303–312 (0).

[18] S. Puligilla, P. Mondal, Role of slag in microstructural development and hardening of fly ash-slag geopolymer, Cement Concr. Res. 43 (2013) 70–80.

[19] S. Zhang, A. Keulen, K. Arbi, G. Ye, Waste glass as partial mineral precursor in alkali-activated slag/fly ash system, Cement Concr. Res. 102 (2017) 29–40.

[20] B.Y. Lee, C.-G. Cho, H.-J. Lim, J.-K. Song, K.-H. Yang, V.C. Li, Strain hardening fiber reinforced alkali-activated mortar – a feasibility study, Constr. Build. Mater. 37 (2012) 15–20.

[21] M. Ohno, V.C. Li, A feasibility study of strain hardening fiber reinforced fly ash-based geopolymer composites, Constr. Build. Mater. 57 (2014) 163–168.

[22] M. Ohno, V.C. Li, An integrated design method of Engineered Geopolymer Composite, Cement Concr. Compos. 88 (2018) 73–85.

[23] B. Nematollahi, J. Sanjayan, F.U. Ahmed Shaikh, Tensile strain hardening behavior of PVA fiber-reinforced engineered geopolymer composite, J. Mater. Civ. Eng. 27 (10) (2015), 04015001.

[24] B. Nematollahi, J. Sanjayan, F.U.A. Shaikh, Matrix design of strain hardening fiber reinforced engineered geopolymer composite, Compos. B Eng. 89 (2016) 253–265.

[25] B. Nematollahi, J. Sanjayan, J. Qiu, E.-H. Yang, Micromechanics-based investigation of a sustainable ambient temperature cured one-part strain hardening geopolymer composite, Constr. Build. Mater. 131 (2017) 552–563.

[26] B. Nematollahi, J. Sanjayan, J. Qiu, E.-H. Yang, High ductile behavior of a polyethylene fiber-reinforced one-part geopolymer composite: a micromechanics-based investigation, Archiv. Civil Mech. Eng. 17 (3) (2017) 555–563.

[27] M. Farooq, A. Bhutta, N. Banthia, Tensile performance of eco-friendly ductile geopolymer composites (EDGC) incorporating different micro-fibers, Cement Concr. Compos. 103 (2019) 183–192.

[28] S. Qian, V.C. Li, Simplified inverse method for determining the tensile strain capacity of strain hardening cementitious composites, J. Adv. Concr. Technol. 5 (2) (2007) 235–246.

[29] V.C. Li, C.K. Leung, Steady-state and multiple cracking of short random fiber composites, J. Eng. Mech. 118 (11) (1992) 2246–2264.

[30] V.C. LI, From micromechanics to structural engineering, Dob. Gakkai Ronbunshu 1993 (471) (1993) 1–12.

[31] B. Nematollahi, J. Qiu, E.-H. Yang, J. Sanjayan, Micromechanics constitutive modelling and optimization of strain hardening geopolymer composite, Ceram. Int. 43 (8) (2017) 5999–6007.

[32] ASTM, C618, Standard Specification for Fly Ash and Raw or Calcined Natural Pozzolan for Use as a Mineral Admixture in Portland Cement Concrete, C618, 2003.

[33] Y. Zuo, M. Nedeljković, G. Ye, Pore solution composition of alkali-activated slag/fly ash pastes, Cement Concr. Res. 115 (2019) 230–250.

[34] S. Zhang, B. Ghiassi, G. Ye, Experimental study on the interface properties of PVA fibers in slag/fly ash based geopolymer pastes, in: 4th International Conference on Service Life Design for Infrastructures, Rilem, 2018, pp. 739–745.

[35] S. Zhang, M. Nedeljković, B. Ghiassi, G. Ye, A comparative study on deflection-hardening behavior of ductile alkali-activated composite, in: International Conference on Strain-Hardening Cement-Based Composites, Springer, 2017, pp. 123–130.

[36] D. Marshall, B. Cox, A J-integral method for calculating steady-state matrix cracking stresses in composites, Mech. Mater. 7 (2) (1988) 127–133.

[37] V.C. Li, Micromechanics and Engineered Cementitious Composites (ECC) Design Basis, Engineered Cementitious Composites (ECC), Springer, 2019, pp. 11–71.

[38] T. Kanda, V.C. Li, Practical design criteria for saturated pseudo strain hardening behavior in ECC, J. Adv. Concr. Technol. 4 (1) (2006) 59–72.

[39] E.-H. Yang, Designing Added Functions in Engineered Cementitious Composites, ProQuest, 2008.

[40] S.A. Bernal, J.L. Provis, V. Rose, R. Mejía de Gutierrez, Evolution of binder structure in sodium silicate-activated slag-metakaolin blends, Cement Concr. Compos. 33 (1) (2011) 46–54.

[41] D. Ravikumar, N. Neithalath, Effects of activator characteristics on the reaction product formation in slag binders activated using alkali silicate powder and NaOH, Cement Concr. Compos. 34 (7) (2012) 809–818.

[42] X. Gao, Q.L. Yu, A. Lazaro, H.J.H. Brouwers, Investigation on a green olivine nano-silica source based activator in alkali activated slag-fly ash blends: reaction kinetics, gel structure and carbon footprint, Cement Concr. Res. 100 (2017) 129–139.

[43] ASTM C 496, Standard Test Method for Splitting Tensile Strength of Cylindrical Concrete, 2011.

[44] ASTM, C 469 Standard Test Method for Static Modulus of Elasticity and Poisson's Ratio of Concrete in Compression, 2010.

[45] TU1404, Towards the Next Generation of Standards for Service Life of Cement-Based Materials and Structures, Main Phase of the Extended Round Robin Testing Programme Testing Protocols, 2016.

[46] Z. Pan, J.G. Sanjayan, B.V. Rangan, Fracture properties of geopolymer paste and concrete, Mag. Concr. Res. 63 (10) (2011) 763–771.

[47] Y. Zhu, S. Xu, Fracture properties of cement paste and mortar: an experimental investigation, Proceedings IA-FraMCoS-6, in: International Assoc. of Fracture Mech. for Concrete and Concrete Structures, Catania, Italy, 1–3, 2007, pp. 17–22.

[48] NEN, 196-1, Methods of Testing Cement–Part 1: Determination of Strength, European Committee for standardization, 2005.

[49] C. Redon, V.C. Li, C. Wu, H. Hoshiro, T. Saito, A. Ogawa, Measuring and modifying interface properties of PVA fibers in ECC matrix, J. Mater. Civ. Eng. 13 (6) (2001) 399–406.

[50] V.C. Li, Engineered Cementitious Composites-Tailored Composites through Micromechanical Modeling, 1998.

[51] E.-H. Yang, S. Wang, Y. Yang, V.C. Li, Fiber-bridging constitutive law of engineered cementitious composites, J. Adv. Concr. Technol. 6 (1) (2008) 181–193.

[52] J. Morton, G. Groves, The effect of metal wires on the fracture of a brittle-matrix composite, J. Mater. Sci. 11 (4) (1976) 617–622.

[53] J. Cook, J. Gordon, A mechanism for the control of crack propagation in all-brittle systems, Proc. R. Soc. Lond. A 282 (1391) (1964) 508–520.

[54] T. Kanda, V.C. Li, Interface property and apparent strength of high-strength hydrophilic fiber in cement matrix, J. Mater. Civ. Eng. 10 (1) (1998) 5–13.

[55] V.C. Li, Postcrack scaling relations for fiber reinforced cementitious composites, J. Mater. Civ. Eng. 4 (1) (1992) 41–57.

[56] K. Rokugo, T. Kanda, H. Yokota, N. Sakata, Applications and recommendations of high performance fiber reinforced cement composites with multiple fine cracking (HPFRCC) in Japan, Mater. Struct. 42 (9) (2009) 1197–1208.

[57] G.P. van Zijl, V. Slowik, R.D. Toledo Filho, F.H. Wittmann, H. Mihashi, Comparative testing of crack formation in strain-hardening cement-based composites (SHCC), Mater. Struct. 49 (4) (2016) 1175–1189.

[58] X. Gao, Q.L. Yu, H.J.H. Brouwers, Reaction kinetics, gel character and strength of ambient temperature cured alkali activated slag–fly ash blends, Constr. Build. Mater. 80 (2015) 105–115 (0).

[59] S. Zhang, Z. Li, B. Ghiassi, S. Yin, G. Ye, Effect of alkali activator modulus on fracture properties of alkali-activated slag/fly ash pastes, in: 15th Congress on the Chemistry of Cements, Prague, Czech Republic, 2019.

[60] S. Zhang, Y. Zuo, Z. Li, G. Ye, Isothermal calorimetric study on heat evolution and of apparent activation energy of alkali-activated slag/fly ash pastes, in: 2th International Conference on Sustainable Building Materials, Eindhoven, the Netherlands, 2019.

[61] D. Ravikumar, N. Neithalath, Reaction kinetics in sodium silicate powder and liquid activated slag binders evaluated using isothermal calorimetry, Thermochim. Acta 546 (2012) 32–43 (0).

[62] V.C. Li, H. Stang, Interface property characterization and strengthening mechanisms in fiber reinforced cement based composites, Adv. Cem. Base Mater. 6 (1) (1997) 1–20.

[63] A. Naaman, G. Namur, H. Najm, J. Alwan, Bond Mechanisms in Fiber Reinforced Cement-Based Composites, MICHIGAN UNIV ANN ARBOR DEPT OF CIVIL ENGINEERING, 1989.

[64] Z. Lin, V.C. Li, Crack bridging in fiber reinforced cementitious composites with slip-hardening interfaces, J. Mech. Phys. Solids 45 (5) (1997) 763–787.

[65] D.A. Lange, H.M. Jennings, S.P. Shah, Relationship between fracture surface roughness and fracture behavior of cement paste and mortar, J. Am. Ceram. Soc. 76 (3) (1993) 589–597.

[66] B. Nematollahi, J. Qiu, E.-H. Yang, J. Sanjayan, Microscale investigation of fiber-matrix interface properties of strain-hardening geopolymer composite, Ceram. Int. 43 (17) (2017) 15616–15625.

[67] E. Yang, V.C. Li, Numerical study on steady-state cracking of composites, Compos. Sci. Technol. 67 (2) (2007) 151–156.

[68] M. Xu, Y. Bao, K. Wu, H. Shi, X. Guo, V.C. Li, Multiscale investigation of tensile properties of a TiO2-doped engineered cementitious composite, Constr. Build. Mater. 209 (2019) 485–491.

[69] V.C. Li, S. Wang, C. Wu, Tensile strain-hardening behavior of polyvinyl alcohol engineered cementitious composite (PVA-ECC), ACI Mater. J. Am. Concr. Inst. 98 (6) (2001) 483–492.

[70] S. Zhang, Q. Feng, D. Wang, G. Ye, Environmental impact evaluation of a slag/fly ash-based strain-hardening geopolymer composite (SHGC), in: ACI/RILEM International Conference on Cementitious Materials and Alternative Binders for Sustainable Concrete, Toulouse, France, 2020.

[71] M. Izquierdo, X. Querol, C. Phillipart, D. Antenucci, M. Towler, The role of open and closed curing conditions on the leaching properties of fly ash-slag-based geopolymers, J. Hazard Mater. 176 (1) (2010) 623–628.

[72] M. Nedeljković, B. Ghiassi, S. van der Laan, Z. Li, G. Ye, Effect of curing conditions on the pore solution and carbonation resistance of alkali-activated fly ash and slag pastes, Cement Concr. Res. 116 (2019) 146–158.

[73] D.L. Kong, J.G. Sanjayan, Effect of elevated temperatures on geopolymer paste, mortar and concrete, Cement Concr. Res. 40 (2) (2010) 334–339.